

## A detailed look into hydrogen electrochemical oxidation on ceria anodes

Tabish, A. N.; Patel, H. C.; Schoonman, Joop; Purushothaman Vellayani, Aravind

**DOI**

[10.1016/j.electacta.2018.05.058](https://doi.org/10.1016/j.electacta.2018.05.058)

**Publication date**

2018

**Document Version**

Accepted author manuscript

**Published in**

Electrochimica Acta

**Citation (APA)**

Tabish, A. N., Patel, H. C., Schoonman, J., & Purushothaman Vellayani, A. (2018). A detailed look into hydrogen electrochemical oxidation on ceria anodes. *Electrochimica Acta*, 283, 789-797. <https://doi.org/10.1016/j.electacta.2018.05.058>

**Important note**

To cite this publication, please use the final published version (if applicable). Please check the document version above.

**Copyright**

Other than for strictly personal use, it is not permitted to download, forward or distribute the text or part of it, without the consent of the author(s) and/or copyright holder(s), unless the work is under an open content license such as Creative Commons.

**Takedown policy**

Please contact us and provide details if you believe this document breaches copyrights. We will remove access to the work immediately and investigate your claim.

# Accepted Manuscript

A detailed look into hydrogen electrochemical oxidation on ceria anodes

A.N. Tabish, H.C. Patel, J. Schoonman, P.V. Aravind

PII: S0013-4686(18)31081-8

DOI: [10.1016/j.electacta.2018.05.058](https://doi.org/10.1016/j.electacta.2018.05.058)

Reference: EA 31844

To appear in: *Electrochimica Acta*

Received Date: 3 July 2017

Revised Date: 30 April 2018

Accepted Date: 7 May 2018

Please cite this article as: A.N. Tabish, H.C. Patel, J. Schoonman, P.V. Aravind, A detailed look into hydrogen electrochemical oxidation on ceria anodes, *Electrochimica Acta* (2018), doi: 10.1016/j.electacta.2018.05.058.

This is a PDF file of an unedited manuscript that has been accepted for publication. As a service to our customers we are providing this early version of the manuscript. The manuscript will undergo copyediting, typesetting, and review of the resulting proof before it is published in its final form. Please note that during the production process errors may be discovered which could affect the content, and all legal disclaimers that apply to the journal pertain.



# A detailed look into hydrogen electrochemical oxidation on ceria anodes

A.N. Tabish<sup>a,d,\*</sup>, H.C. Patel<sup>b</sup>, J. Schoonman<sup>c</sup>, P.V. Aravind<sup>a</sup>

<sup>a</sup>*Department of Process and Energy, Section Energy Technology, Delft University of Technology, 2628CB Delft, The Netherlands*

<sup>b</sup>*Dutch Institute for Fundamental Energy Research, De Zaale 20, 5621 AJ, Eindhoven, The Netherlands*

<sup>c</sup>*Department of Chemical Engineering, Section Materials for Energy Conversion and Storage, Delft University of Technology, The Netherlands*

<sup>d</sup>*Department of Chemical Engineering, University of Engineering and Technology Lahore, Pakistan*

---

## Abstract

Using the Nernst-Planck-Poisson model and a detailed reaction mechanism, we studied the hydrogen electrochemical oxidation on a ceria anode. Resistances caused by surface kinetics, and bulk transport of oxide-ion vacancies and electrons are computed individually to identify the dominant resistive process. The effect of operating conditions like temperature and gas-phase composition on the polarization resistance is evaluated and compared with the experimental data obtained by Electrochemical Impedance Spectroscopy (EIS). The rate-determining step is found to be the charge-transfer reaction in which hydrogen adsorbs at the surface oxide ions and forms hydroxyls along with the charge-transfer to adjacent cerium ions. Based on the rate-determining step, the exchange-current density is also calculated and validated with the experimental data.

*Keywords:* pattern anodes, SOFC, ceria, NPP model, elementary kinetics

---

## 1. Introduction

Ceria is one of the extensively studied mixed ionic and electronic conducting (MIEC) material and inherits outstanding redox properties [1]. It is widely used as a three-way catalyst in automotive industry as well as a promoter for water-gas shift conversion, thermochemical water splitting, and various other catalytic reactions [2]. In the recent years, ceria has gained a considerable attention as an SOFC anode material due to its ability of oxidizing carbon containing fuels [3, 4] and extended electrochemically active area. Doping ceria with trivalent elements like gadolinium and samarium enhances the oxygen vacancy concentration and

---

\*Corresponding author

*Email address:* a.nadeemtabish@tudelft.nl (A.N. Tabish)

hence its ionic conductivity [5]. The electronic conductivity of pure ceria in reducing environment is low, almost 3-4 orders of magnitude lower than nickel at 1000 °C [6]. Therefore, metal/ceria composites are preferred over pure ceria in anode electrode applications.

While nickel/ceria cermets exhibit an excellent electrochemical performance [7, 8], their fundamental electrochemistry is poorly understood. The lack of understanding is mainly due to the complexity of the MIEC nature of ceria and the uncertainty in the relative significance of the two-phase boundary (2PB) between the ceria surface and the gas-phase, and the triple-phase boundary (TPB) between nickel, ceria, and gas-phase. This is unlike conventional nickel/YSZ cermets where electrochemical reactions are only restricted to the TPB between nickel, YSZ, and gas-phase. Recently, Shishkin et al. [9, 10] studied the electrochemical properties of the nickel/ceria cermets using the density functional theory (DFT) and found that the electrochemical fuel oxidation occurs predominantly at the ceria surface than at the TPB. This conclusion was based on the observation that the formation of oxide-ion vacancies is more favorable at the ceria surface than at the TPB. While comparing the performance of nickel/GDC and Au/GDC in a  $H_2/H_2O$  environment, Lei et al. [11] also argued that the electrochemical reactions mainly occur at the GDC surface and the contribution of the TPB is of secondary importance. Therefore, studying the electrochemistry of ceria-based cermets primarily requires the understanding of the ceria electrochemistry itself.

Ceria electrochemistry essentially assimilates the kinetics of the electrochemical reactions at the 2PB and the bulk transport of oxide-ion vacancies and electrons. The overall cell impedance is mainly the cumulative response of these processes. Generally, the ceria-film thickness is kept of the order of nano-meters so that the resistance of ionic transport is small enough to be neglected. The impedance of a thin-film ceria anode, corresponding to what we measure experimentally, can then be categorized into: 1) the drift-diffusion resistance associated with the transport of electrons between the current collector and the reaction sites at 2PB (commonly termed as the current collector spacing), and 2) the surface reaction resistance associated with the charge transfer process at the 2PB. Chen et al. [12] and Ciucci et al. [13] studied these two processes in a reducing environment ( $H_2 - H_2O - Ar$ ) at 550–650 °C using the Nernst-Planck-Poisson (NPP) model. The authors reported that the drift-diffusion resistance is negligibly small if the spacing is less than 10  $\mu m$ , indicating the important role of the reaction resistance. However, with increase in spacing from 10 to 1000  $\mu m$ , the drift-diffusion resistance increases exponentially to become dominant over the reaction resistance at spacing > 1000  $\mu m$ . These results emphasize the need of an efficient current collection mechanism for reaction kinetic studies. Since these studies imply the global reaction kinetics, no conclusion can be made on the reaction mechanism and the charge-transfer process.

Other researchers [6, 14, 15, 16, 17] also studied the ceria electrochemistry in  $H_2 - H_2O$  environments and proposed the reaction mechanisms, charge-transfer processes, and rate-determining step(s). However, these studies do not lead to a consensus on the charge-transfer mechanism and on the rate-determining

elementary step. For example, Zhang et al. [15] and Patel et al. [18] considered a two-step charge-transfer process similar to that of hydrogen oxidation on nickel/YSZ, while Feng et al. [16] proposed a single-step electron transfer from the surface hydroxyl ions to the cerium ions, and DeCaluwe et al. [6] considered charge-transfer at the ceria/YSZ interface. Similarly, El Fallah et al. [14] proposed hydrogen adsorption, while others [15, 16, 6, 18] suggested the charge-transfer as the rate-determining elementary step. Knowledge of the rate-determining step is a key to further improve the anode performance. It also helps deriving the right expression for the exchange-current density – a key parameter to represent the electrochemistry in a fuel cell model. The lack of clarity in the charge-transfer process and the rate-determining step was the motivation for this work.

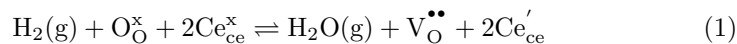
The elementary kinetic modeling approach has been applied for studying the reaction mechanisms and identifying the rate-determining step(s) [19, 20, 21] on nickel anodes. Previously [18], we conducted a preliminary study, using this approach, to identify the rate-determining step for hydrogen electrochemical oxidation on thin-film ceria-pattern anodes. For convenience, both the anionic and the cationic sites were considered equivalent for the adsorption/desorption and the charge-transfer reactions, whereas, DFT studies have shown that the anionic sites are thermodynamically favorable for hydrogen dissociative adsorption than the cationic sites [22]. In this work, we revisited the model developed in ref. ([18]) with a better prediction of the thermo-kinetic parameters and differentiating between the surface sites. Additionally, the bulk transport of oxide-ion vacancies and electrons is also computed using the NPP model to quantify the relative significance of the reaction and diffusion kinetics. The proposed reaction scheme is evaluated over a wide range of temperatures and gas-phase partial pressures. For model validation, results from the EIS of hydrogen oxidation over ceria pattern anodes are used. A sensitivity analysis is carried out to identify the rate-determining step, based on which a model for the exchange-current density is also developed.

## 2. Theoretical modeling

Figure 1 depicts the physical domain of the NPP model.  $\Gamma_5$  refers to the 2PB between ceria and gas-phase where electrochemical reactions occur. Electrons and oxide-ion vacancies produced at  $\Gamma_5$  during the electrochemical oxidation diffuse into the bulk of ceria. The dominant pathways for electron and vacancy transport are from  $\Gamma_5$  to  $\Gamma_4$  and from  $\Gamma_5$  to  $\Gamma_1$ , respectively.  $\Gamma_2$  and  $\Gamma_3$  are the symmetric boundaries. Development of the detailed reaction mechanism and the NPP model are discussed in the following sections.

### 2.1. Development of reaction mechanism

The overall reaction for hydrogen electrochemical oxidation on ceria can be written as (Kröger-Vink notation) [23]:



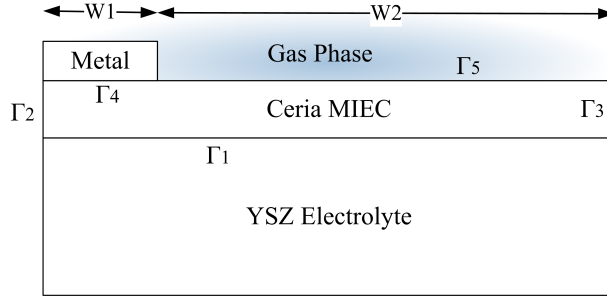
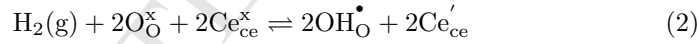


Figure 1: Physical domain of the model

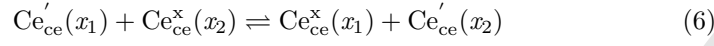
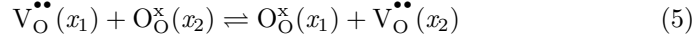
where  $O_O^x$  is an oxide anion residing on an oxide site,  $Ce_{ce}^x$  is a cerium cation ( $Ce^{4+}$ ) residing on a cation site,  $Ce'_{ce}$  is a localized electron at cerium ( $Ce^{3+}$ ), and  $V_O^{\bullet\bullet}$  is an oxide-ion vacancy with an effective charge of 2+. Reaction (1) is the overall oxidation reaction that involves several heterogeneous and surface elementary steps, such as: 1) the adsorption and dissociation of hydrogen on a favorable  $O_O^x$  or  $Ce_{ce}^x$  site, 2) the formation of intermediates such as hydroxyl species, 3) the charge-transfer and transport reactions, and 4) the formation and subsequent desorption of water.

At SOFC operating conditions, the dissociative adsorption of hydrogen on the  $O_O^x$  sites is thermodynamically favorable ( $\Delta H = -165.1$  kJ/mol) compared to that on  $Ce_{ce}^x$  sites [24]. Therefore, it is expected that hydrogen oxidation follows the formation of hydroxyl ions, whereas the hydrogen associative adsorption ( $\Delta H = -3.34$  kJ/mol) or the formation of cerium hydroxide ( $\Delta H = 38.8$  kJ/mol) are either unlikely or unstable. This leads to the following reaction scheme:



Briefly: gaseous hydrogen dissociatively adsorbs on  $O_O^x$  sites and forms two hydroxyl ions ( $OH_O^\bullet$ ) as shown in reaction 2. This reaction also describes the charge-transfer process where two electrons are transferred from  $OH_O^\bullet$  to two  $Ce'_{ce}$ . It is also possible that the hydrogen molecule first dissociates near the oxide ions forming two neutral hydroxyl groups followed by the transfer of two electrons to cerium as suggested in the literature [16]. However, due to the unavailability of the kinetics of each elementary step, the dissociative adsorption and the charge-transfer are considered as a single elementary step. Such an approach has been reported [25]. In the second step, one of the O-H bond weakens and releases a proton which then combines with the neighboring  $OH_O^\bullet$  group to form a water molecule (reaction 3). Water molecules then desorb from oxide sites creating oxide-ion vacancies (reaction 4). Upon formation, these vacancies and electrons diffuse towards their respective boundaries:  $\Gamma_1$  and  $\Gamma_4$ ,

respectively. The transport processes between two nearest neighbor lattice sites,  $x_1$  and  $x_2$ , can be written as:



### 2.2. Surface chemistry

The governing equations for the concentration of surface species are written as:

$$\frac{\partial}{\partial t} c_k = \dot{s}_k \quad (7)$$

$$\dot{s}_k = \sum v_{ki} \left( \overrightarrow{k}_i \prod_{\text{reactant}} c_k^{v_{ki}} - \overleftarrow{k}_i \prod_{\text{product}} c_k^{v_{ki}} \right) \quad (8)$$

where  $k \in \text{O}_{\text{O}}^{\times}, \text{OH}_{\text{O}}^{\bullet}, \text{H}_2\text{O}_{\text{O}}^{\bullet\bullet}, V_{\text{O}}^{\bullet\bullet}, \text{Ce}_{\text{ce}}^{\times},$  and  $\text{Ce}'_{\text{ce}}$ ,  $c_k$  is the molar concentration of surface specie  $k$  ( $\text{mol}/\text{m}^2$ ), and  $\dot{s}_k$  is the net rate of generation ( $\text{mol}/\text{m}^2 \cdot \text{s}$ ). The concentration of specie  $k$  can be expressed as:  $c_k = \Gamma [X_k]$ , where  $\Gamma$  represents the available site density at ceria surface [6] ( $=1.6 \times 10^{-5} \text{ mol}/\text{m}^2$ ) and  $[X_k]$  is the fractional coverage.  $v_{ki}$  is the stoichiometric coefficient of reactant  $k$  in the  $i$ th reaction,  $\overrightarrow{k}_i$  and  $\overleftarrow{k}_i$  are the forward and backward rate coefficients, respectively. To ensure the thermodynamic consistency,  $\overrightarrow{k}_i$  and  $\overleftarrow{k}_i$  are related as:

$$K_i = \frac{\overrightarrow{k}_i}{\overleftarrow{k}_i} = \exp\left(-\frac{\Delta H_i^{\circ} - T \Delta S_i^{\circ}}{RT}\right)$$

Eq. 7 and Eq. 8 are solved simultaneously by applying the conservation of both oxide-ion sites ( $[\text{O}_{\text{O}}^{\times}] + [\text{OH}_{\text{O}}^{\bullet}] + [\text{H}_2\text{O}_{\text{O}}^{\bullet\bullet}] + [V_{\text{O}}^{\bullet\bullet}] = 2$ ) as well as cerium-ion sites ( $[\text{Ce}_{\text{ce}}^{\times}] + [\text{Ce}'_{\text{ce}}] = 1$ ).

### 2.3. Bulk transport

Transport in the bulk of ceria is modeled by explicit consideration of oxide-ion vacancies ( $V_{\text{O}}^{\bullet\bullet}$ ) and electrons ( $\text{Ce}'_{\text{ce}}$ ). Under the assumption that there is no internal source or sink, species conservation in the bulk implies that:

$$\frac{\partial}{\partial t} C_k + \nabla \cdot J_k = 0 \quad (9)$$

where  $k$  refers to the bulk defects: electrons and oxide-ion vacancies,  $C_k$  is the molar concentration ( $\text{mol}/\text{m}^3$ ).  $J_k$  is the species flux ( $\text{mol}/\text{m}^2 \cdot \text{s}$ ) and is related to the gradient of the electrochemical potential ( $\tilde{\mu}_k$ ):

$$J_k = -C_k D_k \nabla \frac{\tilde{\mu}_k}{RT} \quad (10)$$

where  $\tilde{\mu}_k$  is given by:

$$\tilde{\mu}_k = \mu_i^0 + RT \ln(a_k) + z_k F \phi \quad (11)$$

where  $a_k (=C_k/C_k^0)$  is the activity of specie  $k$ . In the dilute limits where species are non-interacting, the charged species flux can be expressed by the Nernst-Planck equation:

$$J_k = -D_k \nabla C_k - \frac{z_k F}{RT} D_k C_k \nabla \phi \quad (12)$$

where  $z_k$  is the charge (+2 for an oxide-ion vacancy and -1 for an electron),  $F$  is the Faraday constant,  $\phi$  is the electric potential (V), and  $D_k$  is the diffusion coefficient ( $\text{m}^2/\text{s}$ ). Under strict neutrality conditions ( $\sum z_k J_k = 0$  and  $\sum z_k C_k = 0$ ), the flux of two coupled charged species can alternatively be represented in terms of the ambipolar diffusion coefficient ( $\mathcal{D}$ ) [26].

$$J_k = -\mathcal{D} \nabla C_k \quad (13)$$

where  $\mathcal{D} = 3D_{V_{\bullet\bullet}} D_{Ce'_{ce}} / (2D_{V_{\bullet\bullet}} + D_{Ce'_{ce}})$ . Eq. 13 is only applicable for the transport of two defects which is the case of transport in pure ceria in a reducing environment. The charge neutrality further leads to the simplification of the Poisson equation.

$$\nabla \cdot (\epsilon \nabla \phi) = -F \sum z_k C_k = 0 \quad (14)$$

where  $\epsilon$  is the permittivity of ceria (F/m). Eqs. 9, 12 and 14 represent a system of coupled partial differential equations, also known as the Nernst-Planck-Poisson (NPP) model.

Solution of the NPP model requires an appropriate definition of the boundary conditions. The simplest boundary condition is at  $\Gamma_2$  and  $\Gamma_3$  which follows that there is no change in the electrochemical potentials, therefore, no change in the defect concentrations and the electric potential. At the MIEC/YSZ interface ( $\Gamma_1$ ) electrons are blocked and oxide-ion vacancies can migrate through. Similarly, at the metal/MIEC interface ( $\Gamma_4$ ) vacancies are blocked and electrons can migrate through. Therefore,  $\frac{\partial}{\partial y} \tilde{\mu}_{Ce'_{ce}} \Big|_{\Gamma_1} = 0$  and  $\frac{\partial}{\partial y} \tilde{\mu}_{V_{\bullet\bullet}} \Big|_{\Gamma_4} = 0$  hold at  $\Gamma_1$  and  $\Gamma_4$ , respectively [13]. The boundary condition at the gas/ceria interface ( $\Gamma_5$ ) is relatively complex because of the complicated interactions between oxide-ion vacancies, electrons, and the gas-phase reactants and products. We assume that the fluxes of vacancies and electrons at  $\Gamma_5$  are given by the rate of reaction 4 and reaction 2, respectively. This follows that  $J_{V_{\bullet\bullet}} = \dot{r}_4$  and  $J_{Ce'_{ce}} = 2\dot{r}_2$ .

### 3. Numerical solution and model validation

We used Matlab® version R2015b and COMSOL® version 5.1 to solve surface concentration and electrochemical potential distribution within ceria bulk, respectively. Table 1 summarizes the simulation parameters and Table 2

Parameter	Value
Current collector width (W1, [ $\mu\text{m}$ ])	25
Ceria exposed width (W2, [ $\mu\text{m}$ ])	125
Temperature [ $^{\circ}\text{C}$ ]	750–850
H <sub>2</sub> sticking coefficient	$4.1 \times 10^{-3}$
H <sub>2</sub> O sticking coefficient	1
Pre-exponent of Reaction (3) rate constant [1/s] [6]	$5 \times 10^9$
Activation energy of Reaction (3) [kJ/mol] [24]	131
$E_{act}$ of H <sub>2</sub> adsorption [kJ/mol]	106.2
$E_{act}$ of H <sub>2</sub> O adsorption [kJ/mol]	0
$V_{\text{O}}^{\bullet\bullet}$ diffusion coefficient [ $\text{m}^2/\text{s}$ ]	$1.96 \times 10^{-10}$
Electron diffusion coefficient [ $\text{m}^2/\text{s}$ ]	$6.46 \times 10^{-9}$
Ceria surface site density [ $\text{mol}/\text{cm}^2$ ]	$1.61 \times 10^{-9}$

Table 1: A summary of the simulation parameters

the thermodynamic properties of gas-phase and surface species. To understand the relative importance of the defect transport and the surface kinetics, three resistance terms, i.e., the cross-plane bulk ionic resistance ( $R_{V_{\text{O}}^{\bullet\bullet}}^{CP}$ ), the in-plane drift-diffusion resistance ( $R_{\text{Ce}'_{\text{ce}}}^{IP}$ ), and the surface reaction resistance ( $R_{chem}$ ) are introduced and defined as [13]:

$$R_{V_{\text{O}}^{\bullet\bullet}}^{CP} = \frac{\langle \tilde{\mu}_{V_{\text{O}}^{\bullet\bullet}} \rangle_{\Gamma_1} - \langle \tilde{\mu}_{V_{\text{O}}^{\bullet\bullet}} \rangle_{\Gamma_5}}{I_{V_{\text{O}}^{\bullet\bullet}}^{CP}} \quad (15)$$

$$R_{\text{Ce}'_{\text{ce}}}^{IP} = \frac{\langle \tilde{\mu}_{\text{Ce}'_{\text{ce}}} \rangle_{\Gamma_4} - \langle \tilde{\mu}_{\text{Ce}'_{\text{ce}}} \rangle_{\Gamma_5}}{I_{\text{Ce}'_{\text{ce}}}^{IP}} \quad (16)$$

$$R_{chem} = \frac{\langle \tilde{\mu}_{V_{\text{O}}^{\bullet\bullet}} \rangle_{\Gamma_5} - \langle \tilde{\mu}_{\text{Ce}'_{\text{ce}}} \rangle_{\Gamma_5}}{I_{V_{\text{O}}^{\bullet\bullet}}^{CP}} \quad (17)$$

here  $\langle \tilde{\mu}_{V_{\text{O}}^{\bullet\bullet}} \rangle$  and  $\langle \tilde{\mu}_{\text{Ce}'_{\text{ce}}} \rangle$  are the average electrochemical potentials of oxide-ion vacancies and electrons at the respective boundaries.  $I_{V_{\text{O}}^{\bullet\bullet}}^{CP}$  is the cross-plane ionic current and  $I_{\text{Ce}'_{\text{ce}}}^{IP}$  is the in-plane electronic current such that  $I_{V_{\text{O}}^{\bullet\bullet}}^{CP} = -I_{\text{Ce}'_{\text{ce}}}^{IP} = z_{V_{\text{O}}^{\bullet\bullet}} F \left( \int J_{V_{\text{O}}^{\bullet\bullet}} dx \right)_{\Gamma_5} = z_{V_{\text{O}}^{\bullet\bullet}} F \left( \int J_{V_{\text{O}}^{\bullet\bullet}} dx \right)_{\Gamma_1}$ .

For model validation, we conducted electrochemical impedance spectroscopy (EIS) experiments with ceria-pattern cells. 1  $\mu\text{m}$  thick ceria patterns (surface area = 0.7414  $\text{cm}^2$ ) were deposited on a YSZ substrate (25 mm diameter and 250  $\mu\text{m}$  thick) using the DC magnetron sputtering (AJA International, ATC 2600 UHV). Details of the sputtering process have been reported previously [27]. Figure 2 illustrates the schematic of the pattern cells and the test assembly.

Species	Enthalpy (kJ/mol)	Entropy (J/mol.K)
H <sub>2</sub>	32.37	175.2
O <sub>2</sub>	27.03	247.6
H <sub>2</sub> O	-210.48	247.02
O <sub>o</sub> <sup>x</sup>	-259.8	68.14
OH <sub>o</sub> <sup>•</sup>	-328.5	69.2
H <sub>2</sub> O <sub>o</sub> <sup>••</sup>	-272	130.5
V <sub>o</sub> <sup>••</sup>	0	0

Table 2: Thermodynamic properties for gas-phase and surface species at 830 °C

For current collection, a square gold mesh (1024 mesh/cm<sup>2</sup>) was used. EIS measurements were conducted using the Gamry Potentiostat (R600).

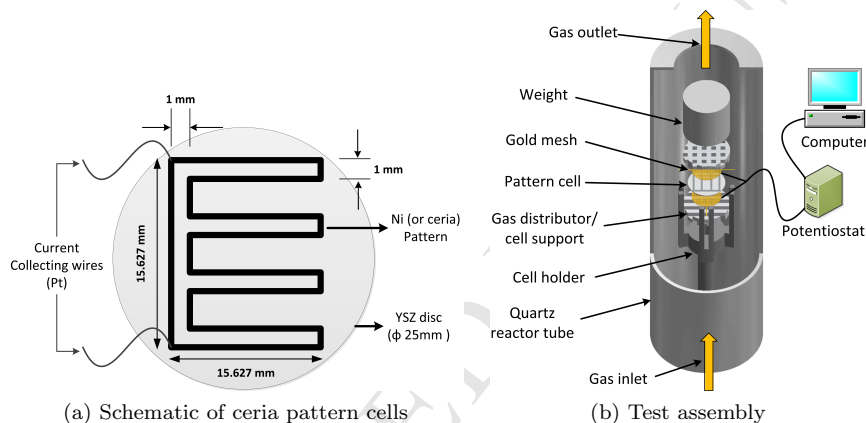


Figure 2: Experimental setup

#### 4. Results and Discussions

Fig. 3 and Fig. 4 show the migration pathways of electrons and oxide-ion vacancies, respectively. Dashed lines represent the electrochemical potential and the solid lines represent the charge flux. The electrons produced at the gas/ceria interface are collected by the metal collector and none of them passes through the ceria/YSZ interface because of the electron blocking nature of the YSZ electrolyte. Similarly, the oxide-ion vacancies produced at the gas/ceria interface converge at the ceria/YSZ interface and none of them pass through the metal/ceria interface because of the ion blocking nature of the metal collector.

The resistances associated with the reaction kinetics and the transport of oxide-ion vacancies and electrons in the ceria are computed from the corresponding electrochemical potential and the current, as given by Eqs. 15–17. The individual contribution of each resistive step to the total electrode resistance

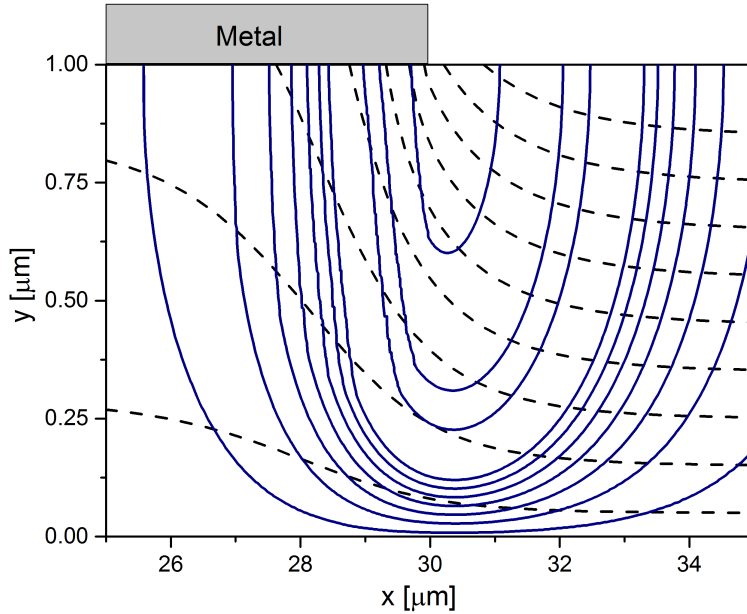


Figure 3: Electronic equi-potential lines (dashed) and charge flux lines (solid) as computed by the Nernst-Planck-Poisson model at 830 °C.

Parameter	Resistance ( $\Omega\text{cm}^2$ )
Surface reaction resistance ( $R_{chem}$ )	72.8
In-plane drift-diffusion resistance ( $R_{Ce'}^{IP}$ )	4.8
Cross-plane bulk ionic resistance ( $R_{V\bullet\bullet}^{CP}$ )	1.3

Table 3: The individual resistive steps computed from the NPP model

is given in Table 3. In line with the previous studies [13, 12], the resistance caused by the ionic and the electronic transport is significantly smaller than the resistance caused by the surface kinetics. This implies that the diffusion process is fast enough to be unlikely to control the cell response at these conditions. Therefore, the rate-determining step is largely related to the reaction kinetics.

For further analysis, the EIS experiments were conducted in a wide range of temperature and gas-phase composition. A representative impedance spectrum at 830°C,  $x_{\text{H}_2} = 0.96$ , and  $x_{\text{H}_2\text{O}} = 0.04$  is shown in Fig. 5. To quantify various resistive and capacitive contributions in the overall cell response, the impedance spectra were deconvoluted using an equivalent circuit as shown in the inset of Fig. 5. This circuit is adopted from Baumann et al. [28] that was originally developed for the thin-film LSCF cathodes. Here, an  $R_{hf} - Q_{hf}$  element is added in series to the original circuit to model the observed high-frequency arc. Decaluwe et al. [29] have also used a similar circuit to model the impedance response of thin-film ceria anodes. The Nyquist and Bode representations –

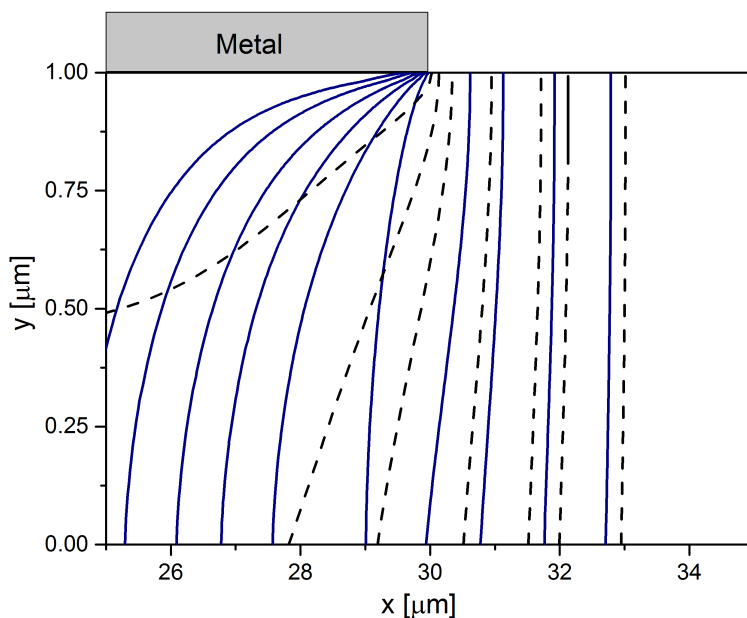


Figure 4: Oxide-ion vacancy equi-potential lines (dashed) and charge flux lines (solid) as computed by the Nernst-Planck-Poisson model at 830 °C.

the experimental spectrum with symbols and final circuit fits with red lines – are shown in Fig. 5a and Fig. 5b, respectively. The circuit fitting fairly overlaps the experimental spectrum except at very low frequencies where some distorted points were observed. The resistances  $R_{chem}$ ,  $R_{int}$ ,  $R_{hf}$ , and  $R_e$  are found to be 76.7, 2.2, 1.3, and 2.1 ( $\Omega\text{cm}^2$ ), respectively.  $R_{chem}$  is related to the electrochemical reaction at the gas/ceria interface. Hereafter, the polarization resistance term is used to refer to  $R_{chem}$ . The capacitances ( $C_{chem}$ ,  $C_{int}$ , and  $C_{hf}$ ) corresponding to three  $R-Q$  elements, as calculated by  $C_i = (R_i^{1-n} Q_i)^{1/n}$ , are  $4.6 \times 10^{-3}$ ,  $4.1 \times 10^{-4}$ , and  $5.2 \times 10^{-6}$  ( $\text{F}/\text{cm}^2$ ), respectively.

Fig. 6 shows the experimental and simulated effect of temperature on the polarization resistance ( $R_{ct}$ ). Similarly, Fig. 7 shows the effect of the hydrogen fraction. The experimental value of hydrogen reaction order is found to be 0.15. It can be seen that the proposed reaction scheme predicts the polarization resistance sufficiently over a wide range of temperature and gas-phase composition. The simulated activation energy is found to be 107.7 kJ/mol that matches well with the experimental value (101.7 kJ/mol).

Simulated fractional coverage of the oxide site species ( $\text{O}_\text{O}^\times$ ,  $\text{OH}_\text{O}^\bullet$  and  $\text{V}_\text{O}^{\bullet\bullet}$ ) as a function of temperature are shown in Fig. 8. The surface coverage of  $\text{H}_2\text{O}_\text{O}$  was very low (of the order of  $10^{-4}$ ), therefore, not shown here. Very low coverage is attributed to the relatively fast  $\text{H}_2\text{O}$  desorption kinetics. As shown in Fig. 8, the coverage of  $\text{OH}_\text{O}^\bullet$  decreases with increase in temperature because, 1) the rate of hydrogen adsorption and hence the hydroxyl formation decreases with

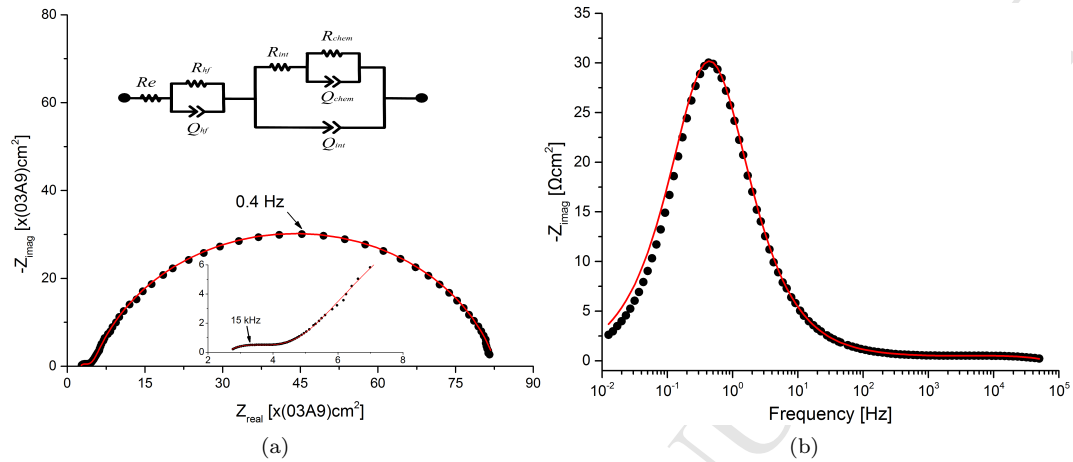


Figure 5: The impedance spectrum and the equivalent circuit model fit at 830°C. The equivalent circuit model itself is shown in (a) inset. Symbols represent the experimental data points and red lines show the corresponding fitting.

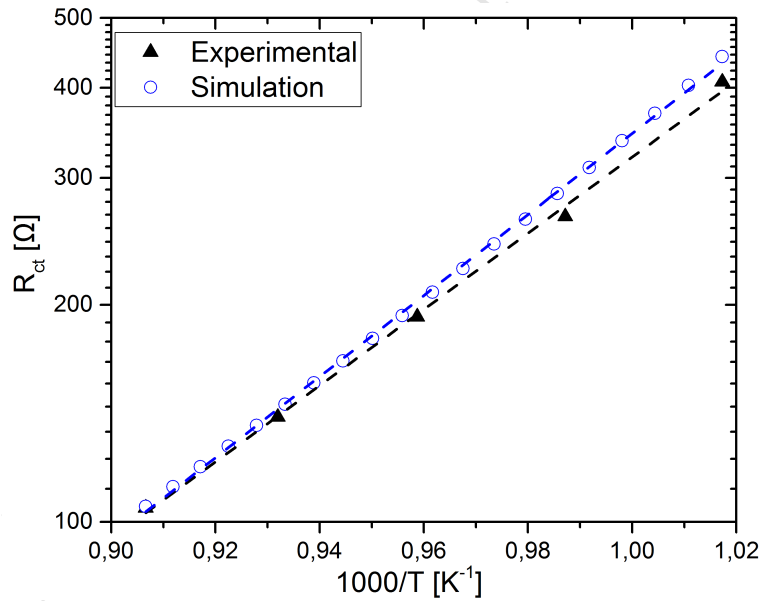


Figure 6: Experimental and simulated Arrhenius plot for H<sub>2</sub>-4%H<sub>2</sub>O gas mixture. Lines are guides to the eye.

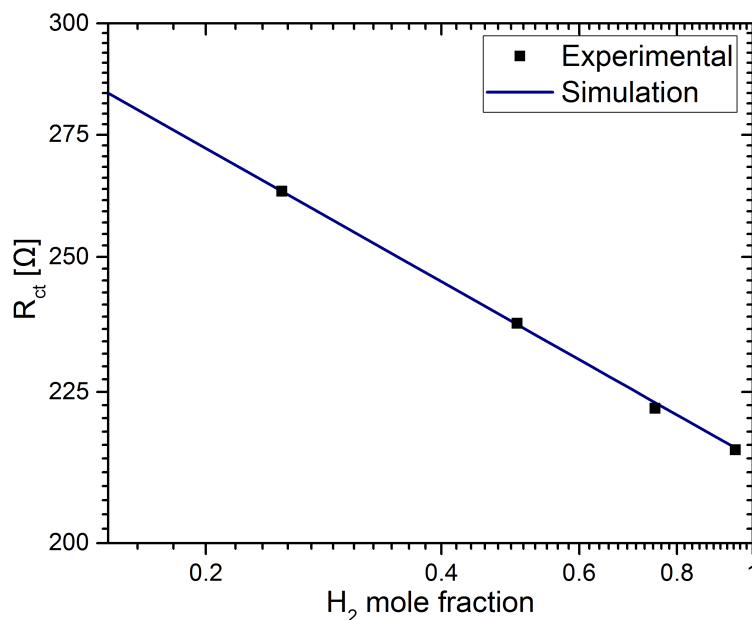


Figure 7: Experimental and simulated resistance as a function of hydrogen fraction (4% H<sub>2</sub>O) at 760 °C.

increase in temperature, and 2) high temperature favors the O-H bond scission that liberates the oxide-ion sites initially covered by the hydroxyl groups. A net increase in O<sub>O</sub><sup>x</sup> coverage, as shown in Fig. 8, is also a result of a large decrease in OH<sub>O</sub><sup>•</sup> coverage compared to a slight increase in V<sub>O</sub><sup>••</sup> coverage. A similar trend is also reported elsewhere [25]. The surface coverage of O<sub>O</sub><sup>x</sup> and OH<sub>O</sub><sup>•</sup> at 700 °C is found to be 0.70 and 0.19, respectively (Fig. 8). When compared with the literature, Zhang et al. [15] found a coverage of O<sub>O</sub><sup>x</sup> and OH<sub>O</sub><sup>•</sup> as 0.75 and 0.25, respectively, with XPS at the same temperature, which are in reasonable agreement with the values found in this work.

#### 4.1. Rate-determining step

Since the resistance caused by the bulk transport is insignificant compared to the resistance caused by the reaction kinetics, rate limitations are globally attributed to the surface kinetics that is in line with the previous studies [13, 12, 30]. The kinetics of elementary steps in the proposed reaction scheme allow us to identify the rate-determining elementary step, which is performed by a sensitivity analysis. The forward rate coefficients of elementary reactions are varied 10% and the resultant polarization resistance is compared with the previous value. The relative sensitivity is defined as:

$$\frac{\Delta R_{chem}/R_{chem}}{\Delta k_m/k_m}$$

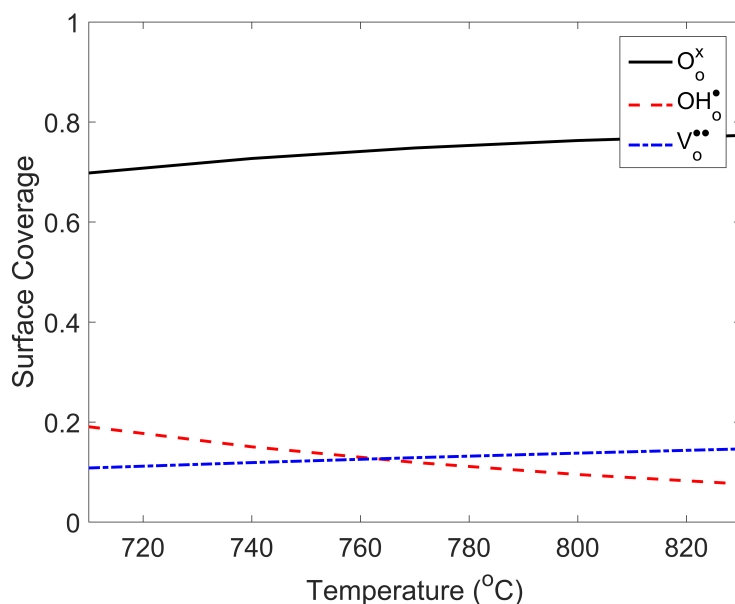


Figure 8: Computed fractional coverage of oxide-site species as a function of temperature for  $H_2$ -4% $H_2O$  gas mixture. A net increase in  $O_o^x$  coverage is a result of a large decrease in  $OH_o^{\bullet}$  coverage.

The relative sensitivity of elementary steps is shown in Fig. 9. It can be clearly seen that the oxidation process is only sensitive to the charge-transfer reaction (reaction 2). This implies that the rate of overall oxidation reaction is determined by the kinetics of reaction 2. Whereas, the formation and desorption of water can then be considered as the equilibrium reactions, proceeding at the same rate as the charge-transfer reaction. In the current reaction scheme, a charge-transfer from surface hydroxyl ions to the neighboring cerium cations is assumed which leads to an effective positive charge on the hydroxyl ions ( $OH_o^{\bullet}$ ) and an effective negative charge on the cerium ( $Ce'_{ce}$ ). The existence of  $OH_o^{\bullet}$  has also been witnessed by Feng et al. [16] through X-ray photoelectron spectroscopy (XPS) measurements. Feng observed that the oxide-vacancy-free (fully oxidized) ceria surface in  $H_2/H_2O$  atmosphere remains mostly in the reduced state, especially under cathodic polarization, leading to the conclusion that the surface hydroxyl groups are effectively positively charged species as they transfer electrons to neighboring cerium ions.

Table 4 summarizes the charge-transfer process and the rate-determining steps reported in the literature. The majority of the studies mentioned in Table 4 also conclude that the charge-transfer step is the rate-determining step, though there is a difference in understanding of how and where this charge transfer takes place. In our previous study [18], despite of the fact that the two-step charge-transfer mechanism was assumed, the rate-determining step was found to be the transfer of electron from hydroxyl to the cerium ions. A

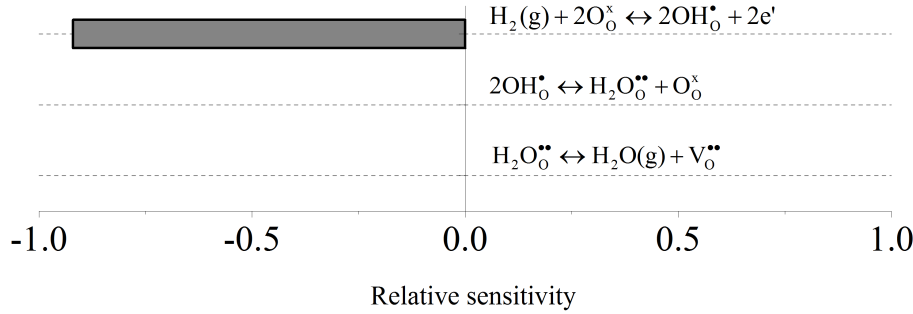


Figure 9: Sensitivity of the charge-transfer resistance to kinetic parameters for elementary reactions at 830 °C

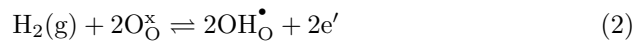
Rate-determining elementary step	Reference
$\text{H}_2(\text{g}) \rightleftharpoons \text{H}_{\text{ads}} + \text{H}_{\text{ads}}$	[14]
$\text{H}_{\text{ads}} + \text{O}_{\text{O}}^{\times} \rightleftharpoons \text{OH}_{\text{O}}^{\bullet} + e'$	[18]
$\text{H}_{\text{ads}} + \text{OH}_{\text{O}}^{\bullet} \rightleftharpoons \text{H}_2\text{O}(\text{g}) + \text{V}_{\text{O}}^{\bullet\bullet} + e'$	[15]
$\text{OH}_{\text{O}}^{\times} \rightleftharpoons \text{OH}_{\text{O}}^{\bullet} + e'$	[16]
$\text{H}_2(\text{g}) + 2\text{O}_{\text{O}}^{\times} + 2\text{Ce}_{\text{ce}}^{\times} \rightleftharpoons 2\text{OH}_{\text{O}}^{\bullet} + 2\text{Ce}_{\text{ce}}^{\prime}$	[25]
$\text{O}_{\text{O}}^{\times}(\text{YSZ}) + \text{Ce}_2\text{O}_3(\text{b}) \rightleftharpoons \text{V}_{\text{O}}^{\bullet\bullet}(\text{YSZ}) + \text{Ce}_2\text{O}_4(\text{b}) + 2e'$	[6]

Table 4: Rate-determining elementary steps reported in the literature

similar conclusion is made before [25]. In addition to the same conclusion on the rate-determining step, Zhenlong et al. [25] also opted for a single elementary step for hydrogen adsorption and the charge-transfer process which is inline with this study. Zhenlong et al. [25] further found that the relative difference of the defect concentration between ceria surface and bulk (up to 100 nm depth) is less than 0.001 % at 1000 °C. Feng et al. [16] also reported a negligible bulk diffusional polarization. Both of these studies also suggest that the bulk diffusion is unlikely to be the rate-determining at SOFC operating conditions. Since, the charge-transfer is found to be the slowest elementary step, lowering the barrier of charge-transfer between  $\text{OH}_{\text{O}}^{\bullet}$  and  $\text{Ce}_{\text{ce}}^{\prime}$  should improve the electrocatalytic activity of ceria.

#### 4.2. Exchange-current density ( $i_o$ )

Since the charge-transfer reaction (reaction 2) is found to be the rate-determining step, a theoretical relationship for the exchange-current density can be derived assuming that all other elementary reactions are in equilibrium. For convenience, the charge-transfer reaction is written as:



Net current density is proportional to the charge-transfer reaction rate and can be written as:

$$\begin{aligned}
i &= \left| \vec{i} \right| - \left| \overleftarrow{i} \right| \\
&= 2F \left[ \vec{k}_1 \exp \left( \frac{2F\beta_a E_{an}}{RT} \right) [\text{O}_\text{O}^\times]^2 \right] - 2F \left[ \overleftarrow{k}_1 \exp \left( -\frac{2F\beta_c E_{an}}{RT} \right) [\text{OH}_\text{O}^\bullet]^2 \right]
\end{aligned} \tag{18}$$

Here, hydrogen concentration is explicitly included in  $\vec{k}_1$  for dimensional consistency: both  $\vec{k}_1$  and  $\overleftarrow{k}_1$  have the dimensions of  $[\text{mol}/\text{cm}^2 \cdot \text{s}]$ . The potential term ( $E_{an}$ ) can be separated into the equilibrium potential ( $E^{eq}$ ) and the overvoltage ( $\eta$ ), so that we finally get a Buttlar-Volmer relation of the form:

$$i = |i_o| \left[ \exp \left( \frac{2F\beta_a \eta}{RT} \right) - \exp \left( -\frac{2F\beta_c \eta}{RT} \right) \right]$$

By definition  $|i_o| \equiv \left| \vec{i}_o \right| = \left| \overleftarrow{i}_o \right|$ , where:

$$\left| \vec{i}_o \right| = 2F \left[ \vec{k}_1 \exp \left( \frac{2F\beta_a E^{eq}}{RT} \right) [\text{O}_\text{O}^\times]^2 \right] \tag{19}$$

and

$$\left| \overleftarrow{i}_o \right| = 2F \left[ \overleftarrow{k}_1 \exp \left( -\frac{2F\beta_c E^{eq}}{RT} \right) [\text{OH}_\text{O}^\bullet]^2 \right] \tag{20}$$

The equilibrium coverage of  $\text{O}_\text{O}^\times$  and  $\text{OH}_\text{O}^\bullet$  can either be obtained by directly solving the rate equation (Eq. 7) or can be extracted from Fig. 8. Alternatively, a potential independent expression can be derived as [31]:

$$|i_o| = \left| \vec{i}_o \right|^{\beta_c} \left| \overleftarrow{i}_o \right|^{\beta_a}$$

On simplification we get:

$$i_o = 2F \left( \vec{k}_1 [\text{O}_\text{O}^\times]^2 \right)^{\beta_c} \cdot \left( \overleftarrow{k}_1 [\text{OH}_\text{O}^\bullet]^2 \right)^{\beta_a} \tag{21}$$

For a typical value of  $\beta_a = \beta_c = 0.5$ , Eq. (21) further simplifies as:

$$i_o = 2F \left( \sqrt{\vec{k}_1 \overleftarrow{k}_1} [\text{O}_\text{O}^\times] [\text{OH}_\text{O}^\bullet] \right) \tag{22}$$

The potential terms in the expression (21) disappears because:

$$\exp(2\beta_a \beta_c F E^{eq} / RT) \exp(-2\beta_a \beta_c F E^{eq} / RT) = 1$$

A further treatment of  $[\text{O}_\text{O}^\times]$  and  $[\text{OH}_\text{O}^\bullet]$  as a function of  $p_{\text{H}_2}$  and  $p_{\text{H}_2\text{O}}$  will reveal the theoretical reaction orders of  $\text{H}_2$  and  $\text{H}_2\text{O}$ . The experimental exchange-current density can be related to the polarization resistance [32]:

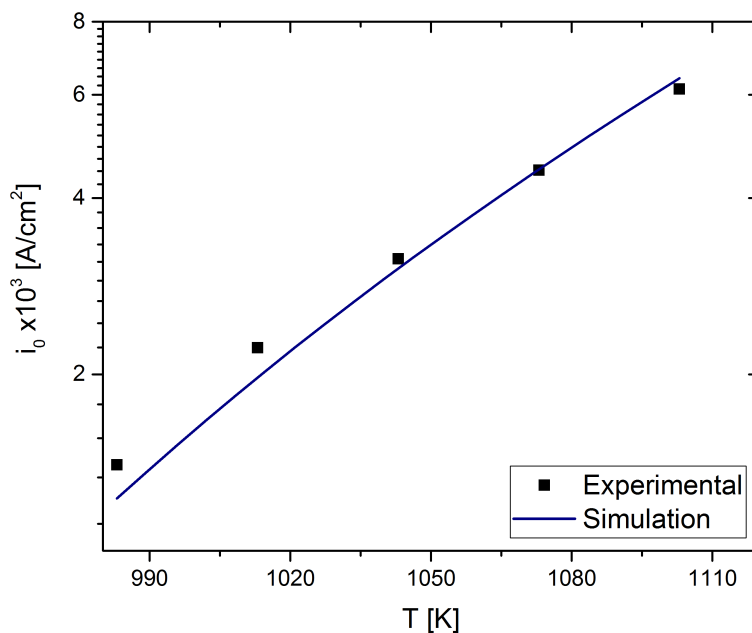


Figure 10: Exchange-current density as a function of temperature for H<sub>2</sub>-4%H<sub>2</sub>O gas mixture

$$i_o = \frac{RT}{zFA_{an}R_{chem}}$$

where  $A_{an}$  indicates the anode active area.  $R_{chem}$  can be obtained by electrochemical impedance spectroscopy. Figure 10 and 11 show the experimental and simulated exchange-current densities as a function of temperature and hydrogen mole fraction, respectively. It can be seen that the simulated exchange-current density reasonably matches the experimental one.

These results can be of a significant importance, as the exchange-current density is the key parameter in fuel cell modeling. While, it is common to use semi-empirical relations in SOFC modeling to address the electrochemistry, the model derived here (Eq. 22) can provide a reliable approximation over a wide range of operating conditions. It is also computationally inexpensive to incorporate this model in a CFD code to obtain the activation overpotential.

## 5. Conclusions

This study presents a detailed mechanistic investigation of the hydrogen electrochemical oxidation on ceria anodes. A reaction scheme is proposed and the NPP model was developed to simulate the resistance associated with the reaction and diffusion kinetics. Kinetic parameters of forward and reverse reactions were coupled considering the thermodynamic consistency and microscopic reversibility

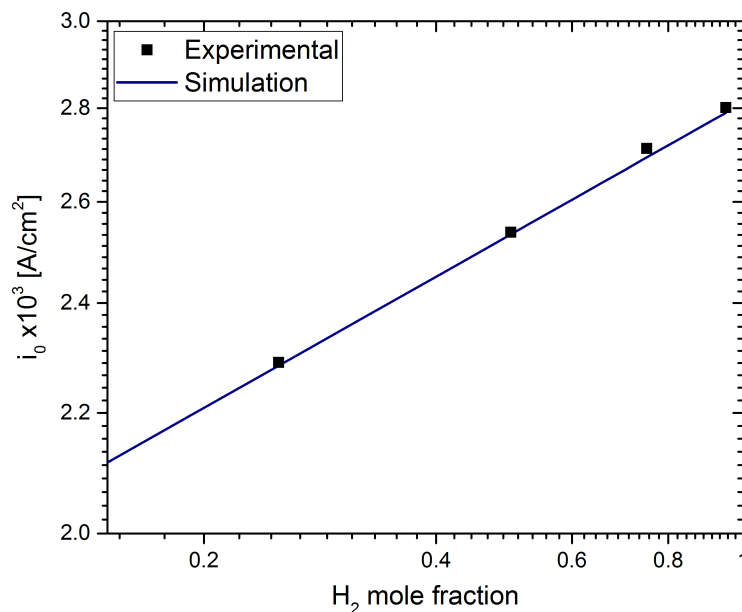


Figure 11: Exchange-current density as a function of hydrogen partial pressure at 760 °C

of the reactions. The effect of operating conditions such as temperature and hydrogen mole fraction were studied in detail.

The simulation has shown that the bulk transport of oxide-ion vacancies and electrons is fast compared to the surface chemistry. Further, a sensitivity analysis has shown that the charge-transfer reaction is the slowest and rate-determining elementary step. Based on this rate-determining step, a quantitative relationship for calculating the exchange-current density is developed and validated with the experimental data. This model can be used to obtain the activation overpotential incorporating the local operating conditions such as temperature and species concentration. This model can also be easily implemented in a CFD code where local conditions are well defined thus avoiding the need of empirically estimating the exchange-current density.

### Acknowledgment

This work has been supported by the University of Engineering and Technology Lahore (UET), Pakistan through a PhD fellowship under Faculty Development Program (FDP). We are thankful to UET for funding this work.

### List of symbols

Symbol	Description
--------	-------------

$A_{an}$	anode active area ( $m^2$ )
$c_k$	concentration of surface species ( $mol/m^2$ )
$C_k$	concentration of bulk defects ( $mol/m^3$ )
$D_k$	diffusion coefficient of bulk defects ( $m^2/s$ )
$\mathcal{D}$	ambipolar diffusion coefficient ( $m^2/s$ )
$E^{act}$	activation energy (J/mol)
$E_{an}$	anode potential (V)
$F$	Faraday constant (96485 C/mol)
$i_o$	exchange-current density ( $A/m^2$ )
$J_k$	electrochemical flux ( $mol/m^2.s$ )
$K_i$	equilibrium constant (-)
$R$	gas constant (8.31 J/mol.K)
$R_{chem}$	surface resistance ( $\Omega cm^2$ )
$R_{V\bullet\bullet}^{CP}$	cross-plane ionic resistance ( $\Omega cm^2$ )
$R_{Ce'ce}^{IP}$	in-plane electronic resistance ( $\Omega cm^2$ )
$\dot{s}_k$	net rate of generation of surface species ( $mol/m^2.s$ )
$\Delta S_i$	entropy change of the reaction (J/mol.K)
$T$	temperature (K)
$[X_k]$	fractional coverage (-)
$z_k$	formal charge (-)
$v_{ki}$	stoichiometric coefficient of reactant $k$ in the $i$ th reaction (-)
$\bar{\mu}$	average electrochemical potential (J/mol)
$\phi$	electric potential (V)
$\varepsilon$	permittivity (F/m)
$\beta$	symmetry parameter (-)
$\eta$	Overpotential (V)
$\Gamma$	surface site density ( $mol/m^2$ )

## References

- [1] A. Trovarelli, Catalytic properties of ceria and CeO<sub>2</sub>-containing materials, *Cataly. Rev.* 38 (1996) 439–520.
- [2] T. Montini, M. Melchionna, M. Monai, P. Fornasiero, Fundamentals and catalytic applications of CeO<sub>2</sub>-based materials, *Chem. Rev.* 116 (2016) 5987–6041.
- [3] S. McIntosh, R. J. Gorte, Direct hydrocarbon solid oxide fuel cells, *Chem. Rev.* 104 (2004) 4845–4866.
- [4] S. Park, R. Craciun, J. M. Vohs, R. J. Gorte, Direct oxidation of hydrocarbons in a solid oxide fuel cell: I. methane oxidation, *J. Electrochem. Soc.* 146 (1999) 3603–3605.
- [5] D. A. Andersson, S. I. Simak, N. V. Skorodumova, I. A. Abrikosov, B. Johansson, Optimization of ionic conductivity in doped ceria, *P. Natl. Acad. Sci. USA.* 103 (2006) 3518–3521.

- [6] S. C. DeCaluwe, Quantifying the role of cerium oxide as a catalyst in solid oxide fuel cell, Ph.D. thesis, 2009.
- [7] O. A. Marina, C. Bagger, S. Primdahl, M. Mogensen, A solid oxide fuel cell with a gadolinia-doped ceria anode: preparation and performance, *Solid State Ionics* 123 (1999) 199–208.
- [8] W. H. Kan, V. Thangadurai, Challenges and prospects of anodes for solid oxide fuel cells (sofcs), *Ionics* 21 (2014) 301–318.
- [9] M. Shishkin, T. Ziegler, The electronic structure and chemical properties of a Ni/CeO<sub>2</sub> anode in a solid oxide fuel cell: a DFT+ U study, *J. Phys. Chem. C* 114 (2010) 21411–21416.
- [10] M. Shishkin, T. Ziegler, Direct modeling of the electrochemistry in the three-phase boundary of solid oxide fuel cell anodes by density functional theory: a critical overview, *Phys. Chem. Chem. Phys.* 16 (2014) 1798–1808.
- [11] L. Wang, Model Development for Gadolinia-doped Ceria-based Anodes in Solid Oxide Fuel Cells, Ph.D. thesis, 2014. URL: <http://drum.lib.umd.edu/handle/1903/16103>.
- [12] C. Chen, D. Chen, W. C. Chueh, F. Ciucci, Modeling the impedance response of mixed-conducting thin film electrodes, *Phys. Chem. Chem. Phys.* 16 (2014) 11573–11583.
- [13] F. Ciucci, W. C. Chueh, D. G. Goodwin, S. M. Haile, Surface reaction and transport in mixed conductors with electrochemically-active surfaces: a 2-D numerical study of ceria, *Phys. Chem. Chem. Phys.* 13 (2011) 2121–2135.
- [14] J. El Fallah, S. Boujana, H. Dexpert, A. Kiennemann, J. Majerus, O. Touret, F. Villain, F. Le Normand, Redox processes on pure ceria and on Rh/CeO<sub>2</sub> catalyst monitored by X-ray absorption (fast acquisition mode), *J. Phys. Chem.* 98 (1994) 5522–5533.
- [15] C. Zhang, Y. Yu, M. E. Grass, C. Dejoie, W. Ding, K. Gaskell, N. Jabeen, Mechanistic studies of water electrolysis and hydrogen electro-oxidation on high temperature ceria-based solid oxide electrochemical cells, *J. Am. Chem. Soc.* 135 (2013) 11572–11579.
- [16] Z. A. Feng, F. El Gabaly, X. Ye, Z.-X. Shen, W. C. Chueh, Fast vacancy-mediated oxygen ion incorporation across the ceria-gas electrochemical interface, *Nat. Commun.* 5 (2014).
- [17] H. Patel, A. Tabish, F. Comelli, P. Aravind, Oxidation of H<sub>2</sub>, CO and syngas mixtures on ceria and nickel pattern anodes, *Appl. Energ.* 154 (2015) 912–920.
- [18] H. Patel, A. Tabish, P. Aravind, Modelling of elementary kinetics of H<sub>2</sub> and CO oxidation on ceria pattern cells, *Electrochim. Acta* 182 (2015) 202–211.

- [19] M. Vogler, A. Bieberle-Hütter, L. Gauckler, J. Warnatz, W. G. Bessler, Modelling study of surface reactions, diffusion, and spillover at a Ni/YSZ patterned anode, *J. Electrochem. Soc.* 156 (2009) B663–B672.
- [20] W. G. Bessler, S. Gewies, M. Vogler, A new framework for physically based modeling of Solid Oxide Fuel Cells, *Electrochim. Acta* 53 (2007) 1782–1800.
- [21] V. Yurkiv, A. Utz, A. Weber, E. Ivers-Tiffée, H.-R. Volpp, W. G. Bessler, Elementary kinetic modeling and experimental validation of electrochemical CO oxidation on Ni/YSZ pattern anodes, *Electrochim. Acta* 59 (2012) 573–580.
- [22] H.-T. Chen, Y. M. Choi, M. Liu, M. Lin, A theoretical study of surface reduction mechanisms of CeO<sub>2</sub> (111) and (110) by H<sub>2</sub>, *ChemPhysChem* 8 (2007) 849–855.
- [23] F. A. Kroger, *The Chemistry of Imperfect Crystals*, 1st edition ed., North-Holland, 1964.
- [24] H. A. Hansen, C. Wolverton, Kinetics and thermodynamics of H<sub>2</sub>O dissociation on reduced CeO<sub>2</sub>(111), *J. Phys. Chem. C* 118 (2014) 27402–27414.
- [25] Z. Zhao, M. Uddi, N. Tsvetkov, B. Yildiz, A. F. Ghoniem, Redox kinetics study of fuel reduced ceria for chemical looping water splitting, *J. Phys. Chem. C* 30 (2016) 16271–16289.
- [26] Y. Chiang, D. Birnie III, W. Kingery, *Physical ceramics*, Wiley, New York, 1997.
- [27] H. Patel, V. Venkataraman, P. Aravind, Nickel pattern anodes for studying soft electrochemistry, in: *Advances in Solid Oxide Fuel Cells IX*, 4, John Wiley & Sons, 2013, p. 89. doi:10.1002/9781118807750.ch8.
- [28] F. S. Baumann, J. Fleig, H.-U. Habermeier, J. Maier, Impedance spectroscopic study on well-defined (La, Sr)(Co,Fe)O<sub>3-δ</sub> model electrodes, *Solid State Ionics* 177 (2006) 1071–1081.
- [29] S. C. DeCaluwe, A. M. Suresh, G. S. Jackson, Experimental characterization of thin-film ceria solid oxide fuel cell anodes, in: *ECS Transactions*, volume 16, The Electrochemical Society, 2009, pp. 235–251. doi:10.1149/1.3242239.
- [30] F. Ciucci, Y. Hao, D. G. Goodwin, Impedance spectra of mixed conductors: a 2d study of ceria, *Phys. Chem. Chem. Phys.* 11 (2009) 11243–11257.
- [31] J. Maier, *Physical chemistry of ionic materials: ions and electrons in solids*, John Wiley & Sons, 2004.
- [32] M. E. Orazem, B. Tribollet, *Electrochemical impedance spectroscopy*, volume 48, John Wiley & Sons, 2011.